Unveiling the complex wear sequence of a directed energy deposited 316L+WC hierarchical composite against alumina

Tommaso Maurizi Enrici[1], Daniele Mario[1], Olivier Dedry[1], Sylvie Castagne[2], Anne Mertens[1], Jérôme Tchoufang Tchuindjang[1]*

[1]University of Liège, Aerospace and Mechanical Engineering Dpt., Metallic Materials Science (MMS) unit
Quartier Polytech 1, Allée de la Découverte 13 (B52) - 4000 Liège, (Belgium)

[2]KU Leuven, Department of Mechanical Engineering and Flanders Make@KU Leuven-M&A
Celestijnenlaan 300 - 3001 Leuven, (Belgium)

*Email: j.tchuindjang@uliege.be

Abstract

In this work, the addition of 20 vol. % of tungsten carbide (WC) to 316L powder processed by direct energy deposition (DED) leads to a hierarchical composite. The modified austenitic microstructure is reinforced by partially dissolved WC, and by a network of solidification carbides. Wear tests for DEDed composite sliding against alumina were carried out, highlighting a cyclical wear regime different from the steady state one achieved on the reference DEDed 316L under similar conditions. The wear behaviour of the DEDed composite sliding against alumina was investigated when considering significant variations of both the friction coefficient (CoF) and the penetration depth (PDe). A novel approach based on interrupted wear tests was applied to better understand the role of the complex hierarchical microstructure of the DEDed composite on its wear behaviour. The wear tracks were analysed through scanning electron microscopy and profilometer at the different stages. This approach allows to observe the evolution of the wear rate with the progress of the test and to identify the corresponding mechanisms that involve adhesive, abrasive and oxidative wears. The influence of WC reinforcements, of the composite matrix or of the counterbody considered solely or in association under dry sliding conditions are discussed thus helping to unveil the complex wear sequence of the DEDed composite. The interrupted wear tests approach also helps to highlight the contribution of the short run-in period and that of the subsequent cyclical regime to the wear rate while considering repeated compaction, breakdown and reformation of a protective tribolayer.

Keywords: Directed energy deposition, Metal matrix composite, Dry sliding interrupted tests, Wear cyclical regimes, Wear mechanisms

1. Introduction

Austenitic stainless steels have widespread applications in aerospace, biomedical and chemical industry due to their excellent corrosion resistance and suitably high ductility. Among these alloys, 316L stainless steel (SS316L) has attracted particular attention for its good plasticity, toughness, weldability and excellent corrosion resistance in oxidizing and reducing media [1–3]. Consequently, this attention has been translated into a large number of publications, including applications of SS316L in the growing additive manufacturing (AM), also known as three-dimensional (3D) printing field [4–6]. Indeed, AM is gaining wide acceptance in diverse industries for the manufacturing of metallic components due to the potential decrease of the wastes and to the improvement of the mechanical properties by the kinetics specific to AM [7–9]. Furthermore, in AM, metallic materials can be improved by combining different feedstock during fabrication in order to enlarge their range of application with the formation of novel alloys and composites [10–13].

316L exhibits good potentialities for this purpose since its relatively low strength and poor abrasion performance have prevented its application in harsh tribological environments. The enhancement of its wear resistance can be achieved by the introduction of hard reinforcements such as ceramics during fabrication by AM techniques, thus creating metal matrix composites (MMCs) with improved tribological and mechanical properties [12,14]. Among AM techniques, directed energy deposition (DED) is particularly suitable for the manufacturing of metal coatings or thick deposits, allowing for a large variability in raw materials [8,13,15–17]. During DED process, extremely high cooling rates and the interactions between molten metal and reinforcements lead to complex hierarchical microstructures and to enhanced properties that are not brought only by a composite effect but by the complex combination of different mechanisms [10,15,18].

Various investigations have considered tungsten carbide (WC) as reinforcement within a composite processed by AM with metallic matrix either made of Fe-based, Ni-based or Al-based alloys, due to the high hardness and good wettability of WC [10,11,16,19,20]. Depending on the volume percentage, WC addition modifies the solidification route of these alloys, leading to new microstructures composed of partially dissolved WC particles and a matrix reinforced by new solidification carbides [10,15,16,18–

20]. Where the tribological behaviour of these alloys was investigated [19–25], the attention was focused on the variation of the wear resistance as function of the test parameters, i.e. temperature, load, sliding speed. This approach is suitable to simulate industrial operating conditions when the testing parameters and setup of the test are close to the actual application conditions [24]. Otherwise, it is limited in the understanding of the wear sequence by considering only post-mortem observations. Therefore, variations of the wear mechanisms or of their relative amplitude with the progress of the test are difficult to detect since observable tribological features (i.e. grooves, oxides, adhered material) are either mixed or hidden by the last main wear mechanism [26–28]. Furthermore, for MMC and complex hierarchical materials as obtained in DED, the understanding of the respective contribution of the large reinforcements and of the reinforced matrix on the wear resistance [12,15,17] is essential in order to tailor the microstructures, e.g. by controlling the characteristics of the initial reinforcement particles prior to fabrication [13,16,23,26]. Attempts in that respect have been done e.g. by Zou et al. [29] who demonstrated that the refining of SiC particles down to nanoscale in the L-PBF (Laser-Powder bed fusion) 316L + SiC composites led to a significant improvement in the tensile and wear properties of the MMC. However, these authors did not investigate in detail the phenomena that occur during the wear tests. Similarly, Nartu et al. [30] studied Ni-rich and carbon-doped in situ MMC fabricated by L-DED while Xiao et al. [19] investigated the DED of WC-Fe composite coatings. Both works established a correlation between the overall wear rate and the hardness. Nevertheless, none of the above works considered the variation of the friction coefficient (CoF) or the complex wear sequence during the test.

The same statement applies to the work of Sun et al. [20] who consider ceramic reinforced Al matrix composites. Complex curves are observed for the CoF during wear tests, but the authors again relate the improved wear behaviour only to the nature and hardness of the ceramic reinforcements.

Only few works have focused on elucidating the dynamics during wear tests on complex materials [31–35]. Indeed, during long tests, the wear behaviour of multiphase materials often exhibits a succession of different wear mechanisms [17,22,26,27,34,36]. Furthermore, the test setup itself and the characteristics of the constitutive phases (i.e. morphology, nature and thermal stability) strongly influence the sequence of wear mechanisms. Indeed, evolving mechanical and chemical interactions

between the phases of the tested material, on the one hand, as well as counterbody and wear debris, on the other hand, lead to an increased complexity of the wear process results [6,31,32,34,37].

Moreover, dry sliding conditions can also lead to variations in the CoF values that are related to changes within the wear mechanisms. Such phenomena need to be well understood, especially when CoF variations take the form of a cyclical regime. The work by Zhu et al. [38], which deals with the manufacturing and the characterization of a H13 tool steel processed by DED and tested at very low sliding speed (26 mm/s) under a 20N load, allows significant variations of the CoF. However, the wear tests carried out for 1800 s show no cyclical wear regime. In the recent study by [39] on a MMC processed by L-PBF, CoF variations related to change of wear mechanisms under dry sliding occur. Nevertheless, the authors focus on the decrease of the average value of CoF with increasing amount of SiC, saying nothing about local variations of the CoF. In the case of MMCs processed by DED using Ti6Al4V as base material with either TiC [40] or TiN [41] as reinforcements, which exhibit significant changes within the value of CoF during wear tests, focus has been made on the steady state wear regime achieved when the wear rate becomes constant, or on the decrease of the average values of CoF with increasing amounts of TiN, respectively. Therefore, no highlighting of the mechanisms explaining CoF variations has been proposed. It can thus be considered that wear is often characterized through the evolution of the average value of the CoF, without focusing on its possible variations, and especially on the correlation between these variations and wear mechanisms.

In this work, a moderate sliding speed is considered, which allows better highlighting of CoF variations. This approach is based on the results of a previous study by Hashemi et al. [37], who enhance the wear behaviour of a DEDed tool steel for which the sliding speed of 10 cm/s allows relevant occurrence of CoF variations that seem to be smoothed for a sliding speed five times higher. When considering similar parameters for the wear tests as those set within [37], CoF variations in the form of a cyclical regime have been observed during tribological tests performed on the DEDed SS316L + WC composite. This leads to the development of a novel experimental approach with interrupted wear tests that may help explaining each CoF variation. Furthermore, this approach allows determining the wear phenomena

that trigger the MMC behaviour during wear test, as well as the contribution of the counter-body to the overall tribological behaviour.

This study considers a MMC based on SS316L and 20 vol. % of WC fabricated by DED, whose preparation has been achieved following a process published in a previous work [16]. The wear behaviour using alumina as counterbody is investigated via a series of interrupted pin-on-disc tests. This approach has been motivated by the fact that the regime occurring during wear tests looks cyclical. To the best author's knowledge, such an approach has so far been rarely explored [36]. These tests were performed under the same conditions and strategically stopped at times corresponding to specific variations of the CoF and penetration depth (PDe). This approach helps differentiating the respective contributions of both the reinforcements and the strengthened matrix on the wear behaviour of the composite as the wear test goes on, thus clarifying the evolution of the wear mechanisms. In order to associate the CoF and PDe variations to wear mechanisms and to locate them in the general wear sequence, post-mortem observations of the specimens and counterbody were performed for each of the interrupted tests. Based on the comparison of these results with observations of the wear behaviour of reference DEDed SS316L without reinforcement, the role of the complex hierarchical reinforced microstructure of the DEDed SS316L + WC composite on its improved wear resistance is assessed.

2. Materials and Methods

2.1. Fabrication and sample preparation

This work considers a metal matrix composite coating composed of SS316L and reinforcements of WC particles (20 vol. %). It has been deposited on a SS316L substrate using a 5-axis Irepa DED system with a Nd-YAG laser source. The raw material used for the production of the parts is made of stainless steel 316L and WC powders with a granulometry between 50 and 200 µm, both having a spherical shape. The final dimensions of the three MMC deposits used in this study were 35 × 35 mm side length and 14 mm height. Both the powders morphology and as-built DEDed deposit sizes can be found in Appendix A1. Furthermore, thick stainless steel 316L deposits were fabricated as wear reference samples, with the same DED processing parameters as those used for DEDed composites. Full details regarding the manufacturing conditions can be found in a previous work [16].

After deposition, the cross-section (Fig. 1a) was obtained from the first deposit by electro-discharge machining (EDM), AgieCharmilles CUT E 600, and used for microscopic inspection by scanning electron microscopy (SEM), after being ground flat to obtain smooth surfaces and polished with diamond paste. The other two deposits were used to produce the wear samples. Two 5 mm thick wear specimens per deposit (Fig. 1a) were obtained by EDM. As shown in Fig. 1b, the deposits were cut at 11.3, 6.3 and 1.3 mm of distance to the substrate. These surfaces, perpendicular to the deposition direction, were ground to reach a R_a < 0.2 µm. The same procedure was applied to the 316L reference.

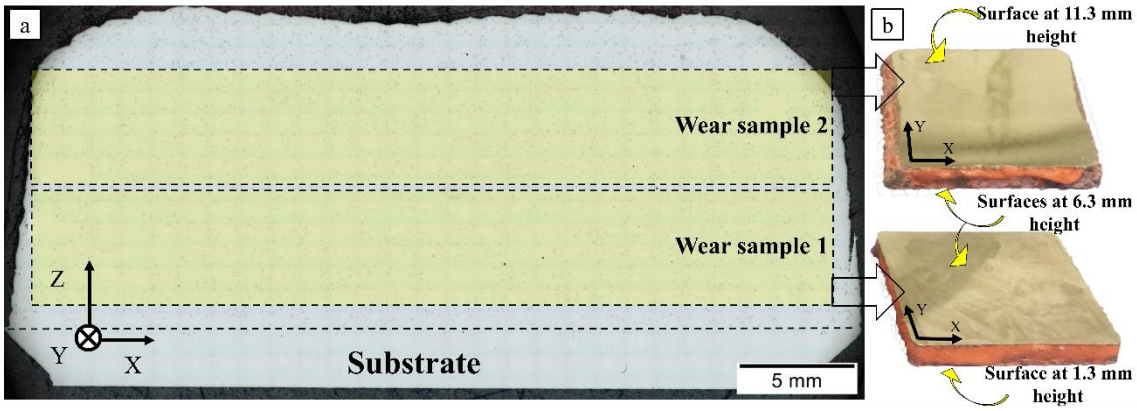

Fig. 1 : The two wear specimens located on the cross-section (a) with the respective surfaces (b).

2.2. Wear tests

Tribological experiments were performed at room temperature (RT) in dry conditions on a CSM high-temperature pin-on-disc tribometer [37]. The composite material was used as disc and an alumina ball

(Al_2O_3) of 6 mm diameter was used as pin. Alumina was chosen as counter-material because it possesses a hardness of 1800HV, which is harder than the test specimen i.e. 350-500 HV [2,5,31]. In addition, using alumina instead of WC might avoid solubilization of composite components into the ball. The whole test campaign was performed on surfaces at 6.3 mm of distance to the substrate (Fig. 1b), under a constant load of 10 N and sliding speed of 10 cm/s, while considering a radius of 9.5 mm for the circular wear track This set of parameter was chosen in accordance with previous tribological studies on 316L and with ASTM G133-95 [1,25]. The height at 6.3 mm from the substrate has been chosen in order to have two surfaces (referred to as 6.3 surfaces) corresponding to the same position from two different wear samples (Fig. 1b) and to avoid microstructural variations due to the heat accumulation [8,42] . CoF and PDe were measured by the tangential or vertical deviation of the pin-on-disc arm sensors, respectively. Moreover, the tests were recorded by a HERO7 Action camera in order to detect variations in acoustic emission [43–45]. Two tests with the same conditions and with a constant test length that corresponds to 22000 laps (named test0) were carried out on one 6.3 surface of the second deposit to check the repeatability of the results and to set the position of the interrupted tests. Then, four interrupted tests were carried out on the two 6.3 surfaces of the third deposit. The lengths of these interrupted tests were set respectively to 750 laps (test1), 9300 laps (test2), 11700 laps (test3) and 15000 laps (test4).

2.3. Characterization methods

The volume loss of the samples was estimated by measuring the wear track profile using an Alicona Infinite Focus G5 optical profilometer, which allows to consider all surface features having sizes greater than the chosen resolution. In addition, the spherical cap of the alumina ball and the corresponding worn volumes were calculated by measuring the diameter and height on the topographies. The images were taken with the ring-light option. The vertical resolution was set at < 410 nm and the horizontal resolution at 7.83 µm. Furthermore, the wear rates were calculated by dividing the worn volume by the sliding distance (m). After the tribological test, top views of the worn surfaces, cross-sections of the wear tracks and debris collected using a carbon sticker were analysed by SEM using both backscattered electron (BSE) or secondary electron (SE) detectors for topographic and chemical contrasts respectively, or energy dispersive x-ray spectroscopy (EDS) for semiquantitative chemical analysis [26].

3. Results

3.1. Microstructure of the 316L+WC composite

In the microstructure of the metal matrix composite, partially dissolved WC reinforcements are well distributed in an austenitic matrix (Fig. 2a) reinforced by a bright network of solidification carbides (Fig. 2b). In a previous work by the present authors [16], an in-depth microstructural characterization has shown that these solidification carbides are of $(W, Cr)_xC_y$ type, and that they result from the partial dissolution of the original WC powders within the metal matrix. In particular, metastable M_4C carbides are observed in the melt pool (Fig. 2c), while M_6C and $M_{23}C_6$ carbides are found in the immediate vicinity of the reinforcements (Fig. 2b) and in the heat affected zone (HAZ) formed due to the reheating of previously solidified material upon the deposition of a new layer (Fig. 2c) [10,16]. These solidification carbides are observed together with a crown of γ-WC_{1-x} carbide and pure W around the WC cores, forming a connection layer between the reinforcements and the matrix (Fig. 2b). On the other hand, reference 316L exhibits a cellular austenitic microstructure (Appendix B, Fig. B.1), where both cells and cell boundaries are austenite [13,14].

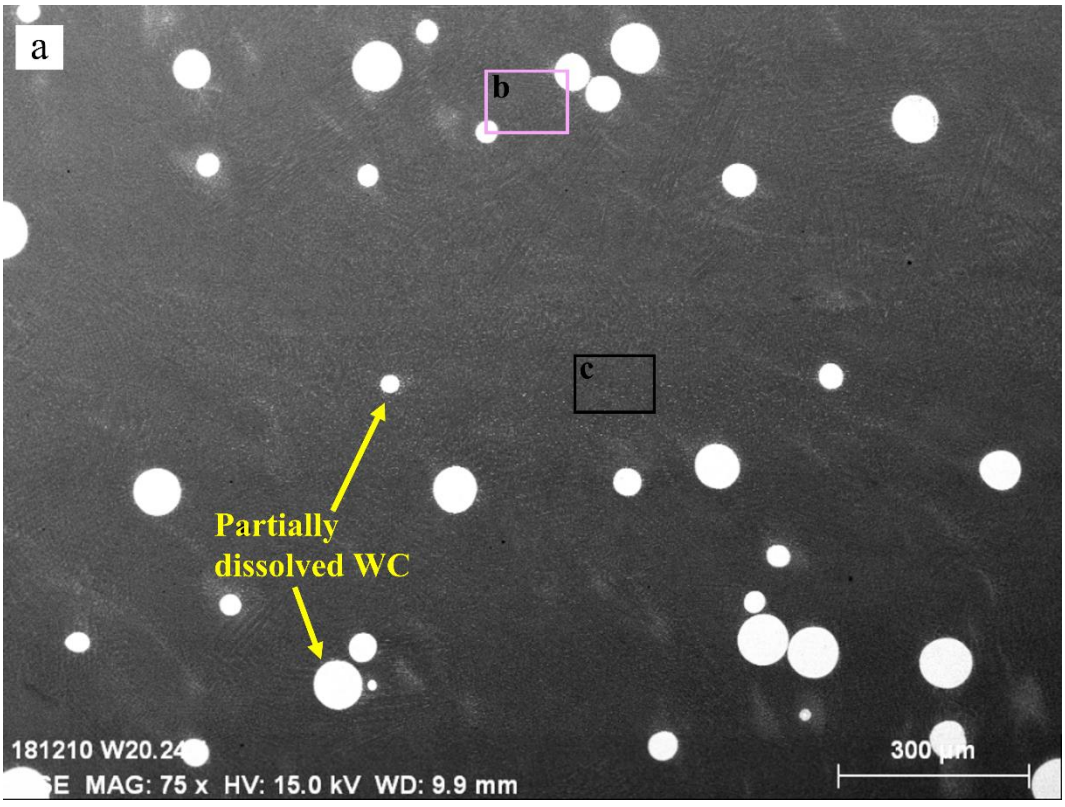

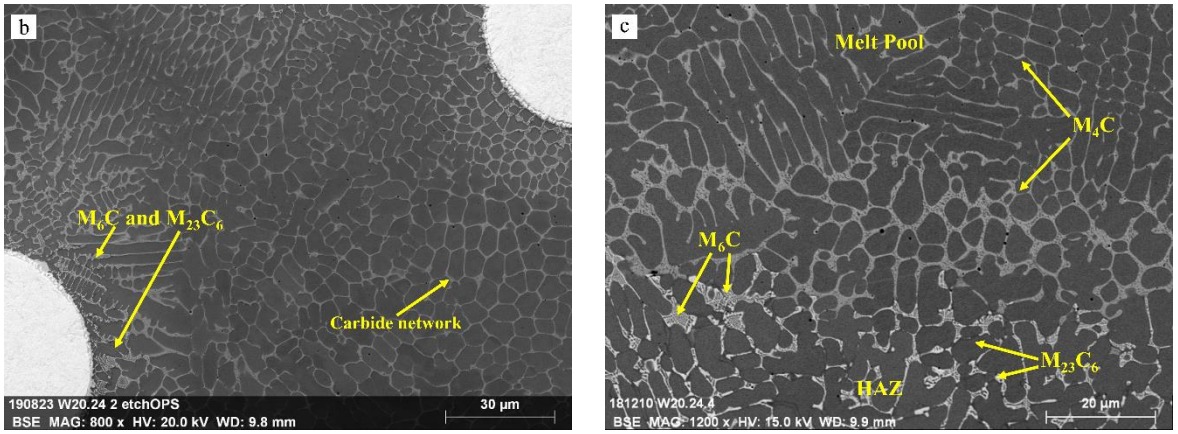

Fig. 2: (a) SEM micrograph of the 316L+20%WC composite. Partially dissolved WC carbides (bright circles) are homogeneously dispersed in a reinforced matrix. (b) Close-up view of (a) showing the immediate vicinity of the partially dissolved WC carbide (light grey) and the network composed of solidification carbides. (c) Another close-up view of (a) focused on the transition between melt pool and HAZ with their respective solidification carbides.

3.2. Evolution of the coefficient of friction and penetration depth during wear tests

Fig. 3 presents the variations of CoF and PDe under sliding contact, indicating that the CoF continuously changed with the running length. Good test repeatability is achieved among the three tested 6.3 surfaces. Fig. 3a (test0) is considered as reference for the values of CoF and PDe in the following description. As shown in Fig. 3a, the CoF has a relatively short run-in period [27,28,46] and then enters a cyclical regime formed by repeated segments. For comparison purposes, the 22000 laps test of the reference 316L is given in Appendix B (Fig. B.2).

The run-in period and the first segment of the cyclical regime in test0 (Fig. 3a) can be divided into six stages, which are related to specific variations of the CoF and the PDe. A further seventh stage corresponds to the beginning of the second segment of the cyclical regime. This division will be used in section 4.2 for the elucidation of the wear sequence considering the observations of section 3.3.

The run-in period is characterized by a sharp increase of the CoF (Fig. 3b and c), followed by a stage characterized by small fluctuations around a CoF of 0.65-0.7. Simultaneously, the PDe exhibits an initial short plateau (stage1) and then a continuous rise (stage2). The run-in period ends after 2200 laps with a sharp increase of CoF up to 0.7-0.75 followed immediately by a sharp decrease to 0.6-0.65 (Fig. 3a and c), while the PDe levels off at 0.3 mm (stage3).

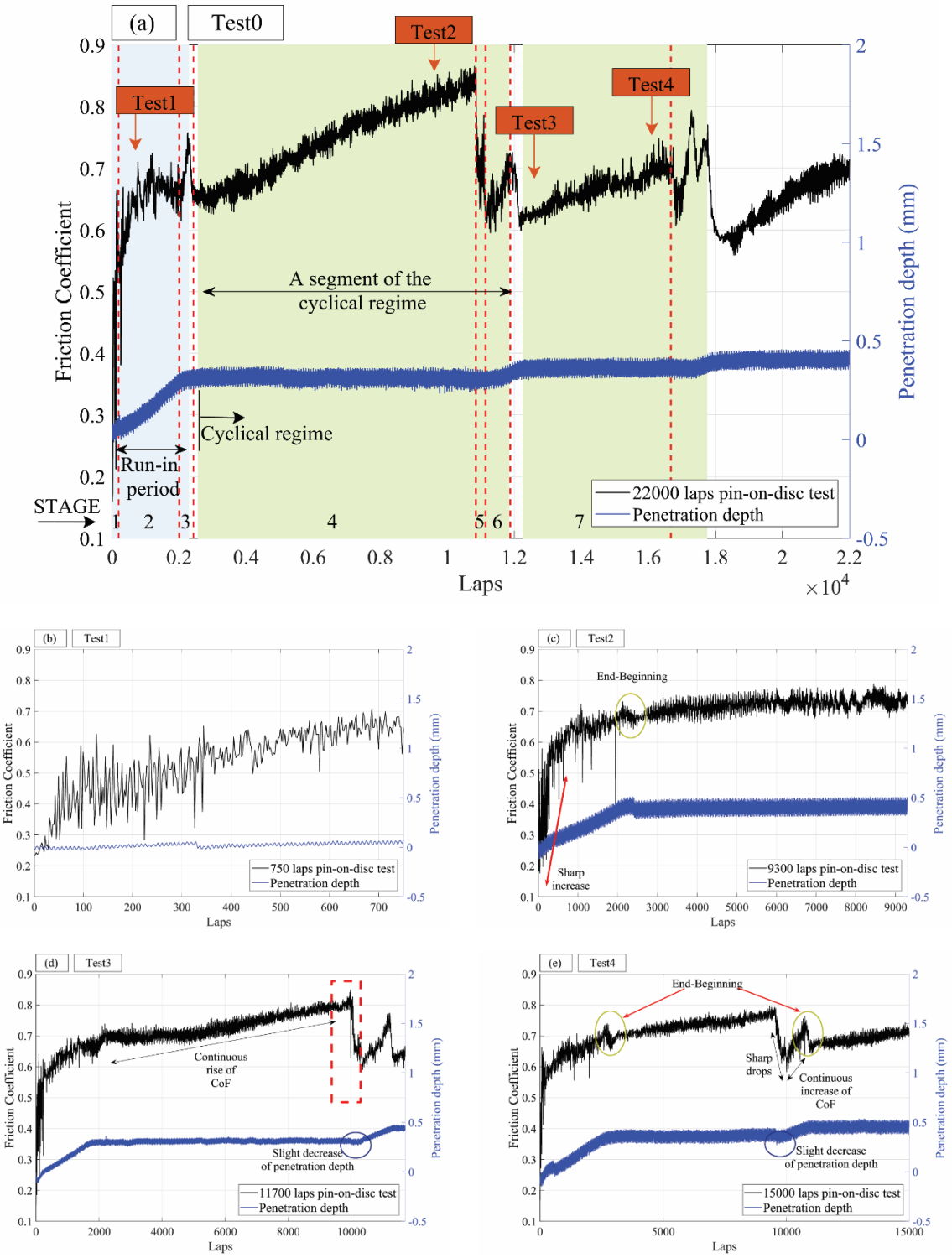

Fig. 3 : Measured friction coefficient (CoF) and penetration depth (PDe) during pin-on-disc tests, at (a) 22000, (b) 750, (c) 9300, (d) 11700 and (e) 15000 laps. In Appendix C available online, a video exhibits the variation of the sound corresponding to the red rectangle of Fig. 3d.

Therefore, the run-in period contributes to almost 90% of the increase of the PDe recorded within the first six stages. This 90% of the wear loss occurs within 10% of the time up to the end of the first cyclical segment. Moreover, the wear loss at the end of stage 6 corresponds to ~75% of the total wear

loss at the end of test0. Then the following stages achieved within the total running length of 22000 laps, which correspond to almost two additional cyclical segments, yield the additional 25% of the total wear, with the final PDe set at 0.45 mm (Fig. 3a).

Almost three successive cyclical segments occur when considering the total running length of 22000 laps, each of them being made of three stages i.e. stages 4 to 6 for the first cyclical segment (Fig. 3a). First, the PDe exhibits a steady value at 0.3 mm while the CoF increases continuously (stage 4). Then, as highlighted in Fig. 3d and 3e, the CoF collapses, whereas the PDe shows a slight decrease, followed by a short plateau (stage 5). The ultimate stage 6 is initially characterized by a continuous rise of the CoF up to 0.7 – 0.75, followed by one or two sharp drops (Fig. 3e). Then there is another increase under a steeper slope before the final decrease of CoF down to 0.6-0.65. Meanwhile, PDe increases from 0.3 mm to a new steady value of 0.45 mm during stage 6 (Fig. 3a), thus ending up with the first segment of the cyclical regime. Stage 7 (Fig. 3a) that is characterized by new variations within both CoF and PDe after stage 6, set up the beginning of the second segment of the cyclical regime. The three segments of the cyclical regime which occur within the total running length of 22000 laps present similar stages. The same relative variation is observed on all 3 segments if only PDe is considered. For CoF, on the other hand, the absolute maximum decreases from 0,85 to 0,75 as the segments progress.

Transitions between the continuous rise and collapse of the CoF (dotted red rectangle in Fig. 3d) can also be characterized by noise, with grinding squeals (Appendix B (Fig. B.3) and Appendix C (video) within the supplementary materials). During sliding, part of the kinetic energy produces waves and oscillations in the bodies, and part of this energy leads to plastic and anelastic deformation of the asperities [44,45]. Energy expends mainly through viscous dissipation, and a combination of adhesion, fracture and chemical reaction. The distribution of energy conversion varies for different applications. Each of these processes provides a mechanism for converting the original kinetic energy to an interim one in the form of vibration and sound, deformation energy, surface energy, tribo-chemical energy and other tribo-emissions [43]. Interestingly, no sound is produced when CoF collapses. Such a phenomenon can be ascribed to decrease of both the friction and the kinetic energy produced by the sliding contact.

3.3. Post-mortem observations

3.3.1. Profilometer measurements

The volume losses of the clad 316L+20% WC composite and of the alumina ball during the pin-on-disc tests are shown in Fig. 4. The wear track of the composite is homogeneous (Fig. 4a) and its volume loss after 22000 laps (1313 m) is 0.581 mm^3. For comparison, the volume loss of a clad SS316L produced with the same fabrication parameters and tested under the same conditions is 11 times higher (6.534 mm^3). The related PDe of 1.35 for a clad SS316L (Appendix B, Fig. B2) is three times higher than that of the composite (Fig. 3a) .As shown in Fig. 4b, the worn volume of the track exhibits an almost linear increase with respect to the number of laps. Moreover, as also observed in works both by Dai et al. [36] and by Downey et al. [44], the wear rate of the specimen first decreases, and then remains stable with prolonged sliding time. This is attributed to the formation of an oxide-like tribolayer. Indeed, for short sliding time, wear debris is generated between the mating surfaces. The surface roughness then increases, leading to higher wear rates. With increasing sliding time, an oxide film can be formed that protects the sliding surface. Furthermore, a worn cap [17,27,31] was observed in every alumina ball after the tests (Fig. 4c). Its size increases with the sliding distance for the four interrupted tests. In contrast, the worn cap of the alumina balls used for the two test0 deviate slightly from this tendency. This can be attributed to the fact that these two tests were carried out on a different 6.3 surface, as will be discussed in section 4.2.2. The wear rate of the alumina ball decreases linearly with the increase in the distance.

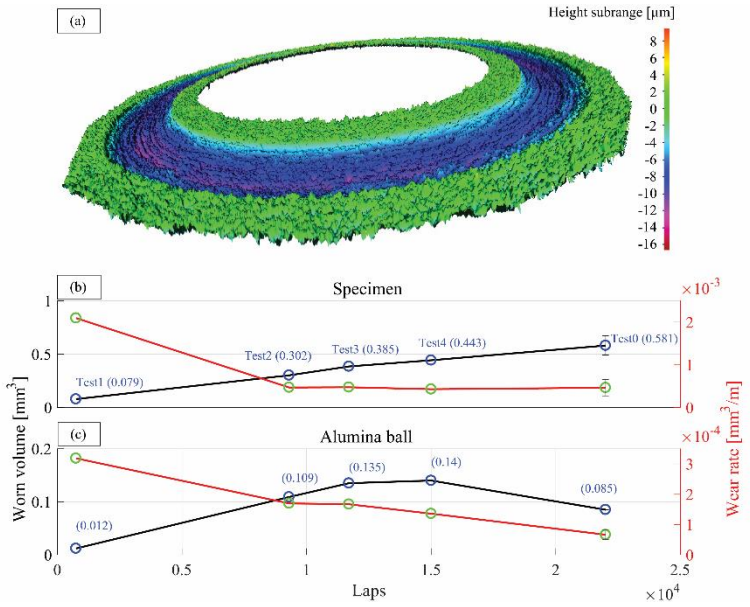

Fig. 4 : (a) 3D topography of the wear surface after 22000 laps pin-on-disc test. Measured worn volumes ((b) wear track and (c) alumina cap) of the five different tests vs the number of laps.

3.3.2. Wear tracks

3.3.2.1. General overview

Fig. 5 shows typical overviews of the worn surfaces for the four successive interrupted pin-on-disc tests and for the complete test carried out over the total length of 22000 laps. As shown in Fig. 5a, the surface away from the tracks is in ground conditions. It is homogeneous with a few crystals of the WC carbides [16] that have been pulled out during preparation, leaving small fractures or cracks. Depending on the length of the test run, the track surfaces exhibit different features, such as delaminated material [3,14,46] (Fig. 5a and b), dark patches of various shapes [31,47] (Fig. 5a, c and d), grooves [25,28,31] (Fig. 5a, b and d), plastic flow [4,14,23,28] (Fig. 5b and d) and adhered material [23,32] (Fig. 5c, d and e). Test2 (Fig. 3c and Fig. 5b) and test4 (Fig. 3e and Fig. 5d) exhibit very similar features of the track surface. Thus, they are assumed to undergo the same wear mechanism.

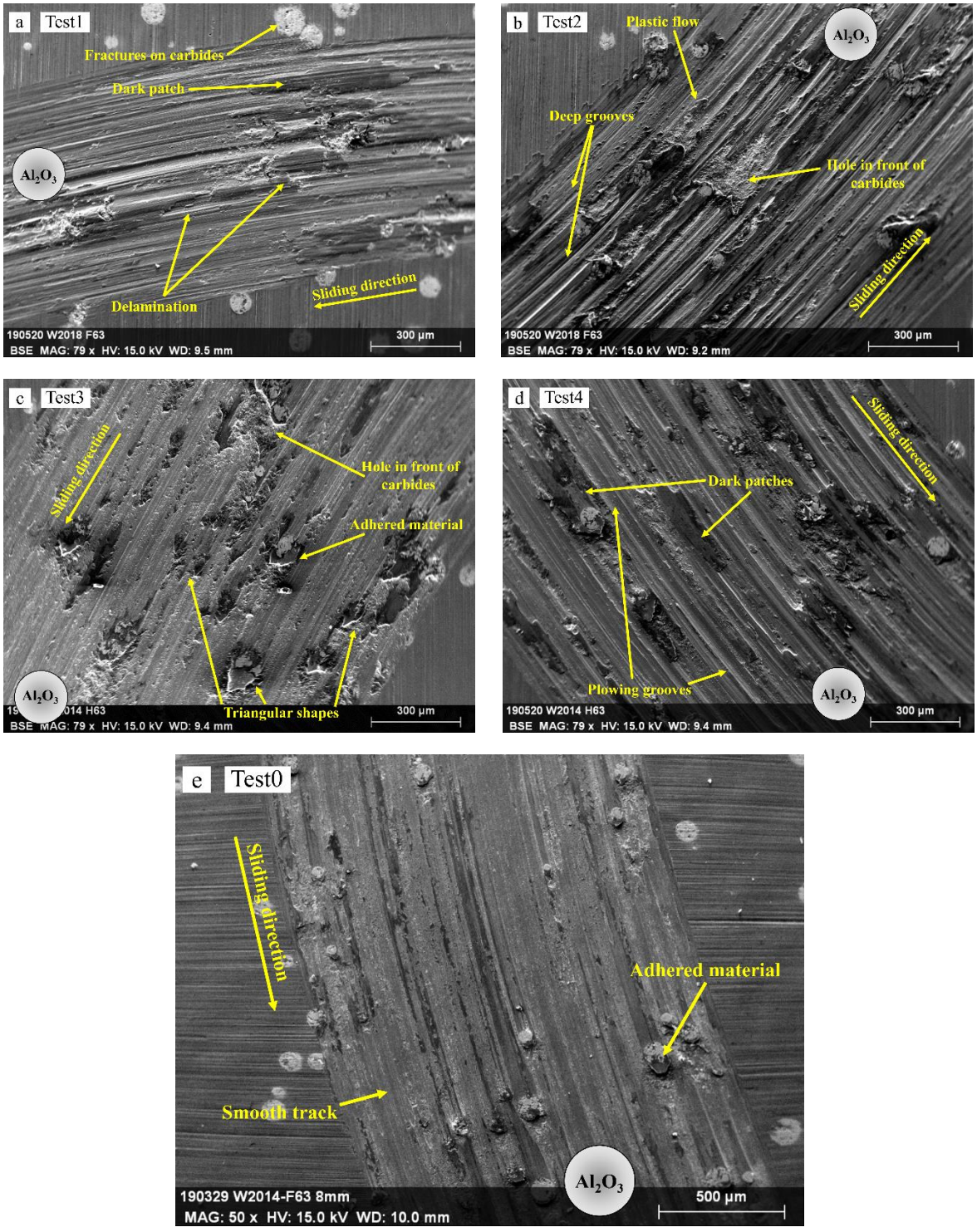

Fig. 5 : The worn tracks (SE mode) after (a) 750, (b) 9300, (c) 11700, (d) 15000 and (e) 22000 laps pin-on-disc test. A sphere represents the alumina ball position while the sample is turning anticlockwise.

3.3.2.2. Run-in period

The track overview of test1 corresponding to the run-in period (Fig. 3b) is characterized by the presence of delamination of material, few grooves and dark patches (Fig. 5a). In Fig. 6a, brittle failures are observed after the material delamination [28]. The dark layer as observed under BSE detector (Fig. 6b), is either well compacted or composed of small debris (Fig. 6a), including small bright WC particles

(Fig. 6b). This dark layer exhibits the same shape as the gap left by the brittle failure. In addition, the dark patches cover both the matrix and the WC carbides (Fig. 6c), filling both the cracked carbides and the grooves within the track. Moreover, these dark patches are O-rich adhesive coatings containing Cr, Fe and Al (Fig. 6e), the relative amount of Al increasing upon WC carbides (Fig. 6d). Therefore, the dark layer is a complex oxide, which is different than another Cr and Fe containing oxide (Fig. 6g and h) that is also observed on the matrix away from the patches.

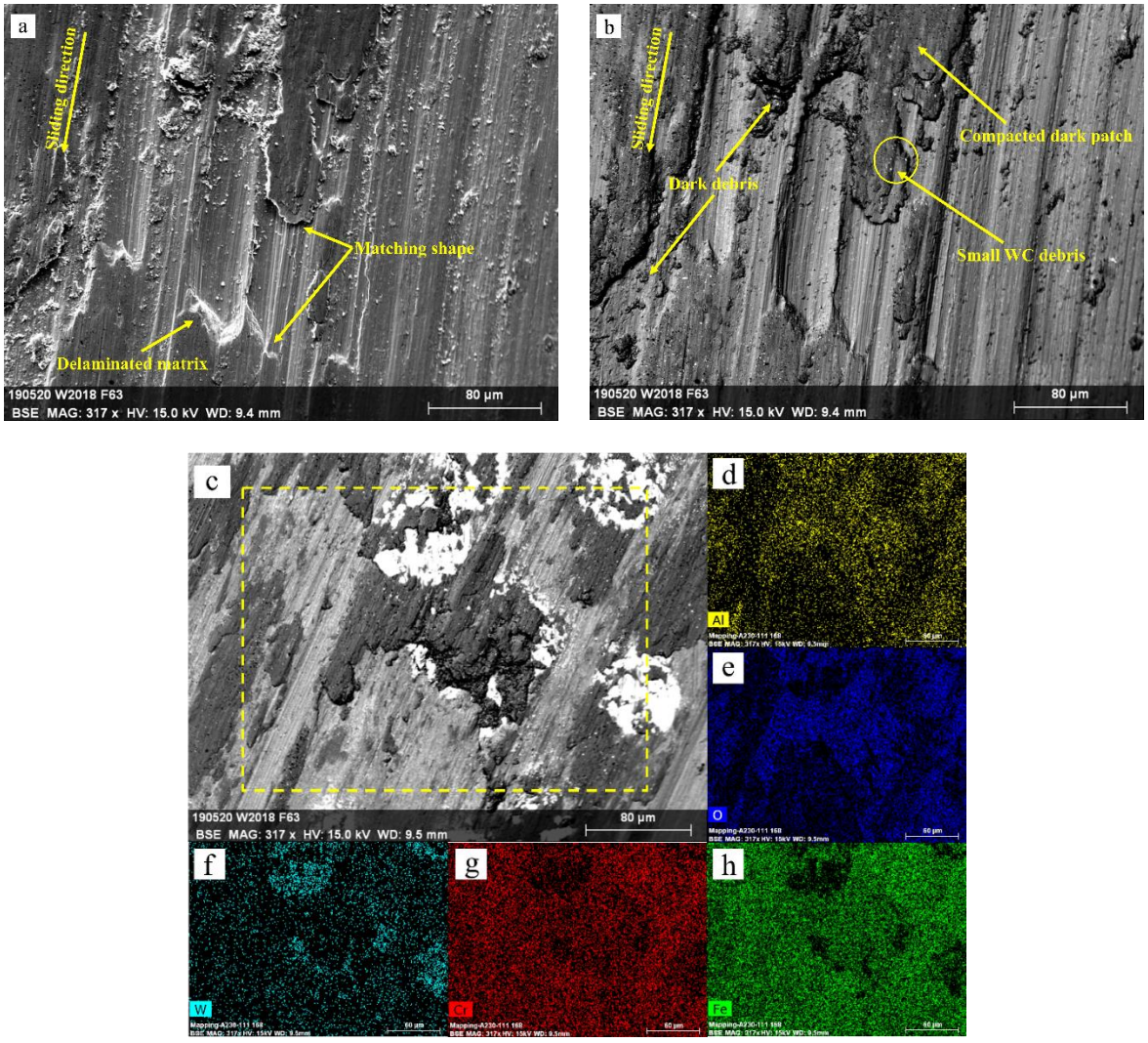

Fig. 6 : (a) SE and (b) BSE micrographs of the typical worn surface of test1 at 750 laps, as observed away from the WC carbides. (c) BSE micrograph of dark patches on the wear track and specifically on the WC carbides with the corresponding EDS analysis (d to h) after test1 at 750 laps). Preferential distribution of both Al (d) and O (e) ahead of WC reinforcements (f) due to the wear phenomenon by WC occurring within the counterbody, while both Cr (g) and Fe (h) show a more homogeneous distribution around the WC reinforcements that corresponds to the composite matrix

3.3.2.3. Cyclical regime: first segment

When increasing the test length up to 9300 laps (Fig. 3c), the track exhibits increased grooving and plastic flow (Fig. 5b), in addition to the adhered material upon WC carbides (Fig. 6c and Fig. 7a).

Cavities are present in front of the WC carbides according to the sliding direction (Fig. 7c and e). The adhered material on the WC carbides corresponds to alumina (Rectangles 2 and 5 in Table 1, Fig. 7d and f), whereas debris inside cavities are made of a mixture of Al, Cr, Fe and W oxides (Rectangles 3, 6 and 7 in Table 1, Fig. 7d and f). In this respect, it is worth noting that the contribution from the neighbour phases to the interaction volume may be high in the case of the isolated debris, due to their size smaller than that of the matrix or of the partially dissolved WC.

As shown in Fig. 7c and e, the matrix located behind the WC carbides according to the sliding direction (Rectangle 1 in Table 1 and Fig. 7d) does not exhibit grooves or plastic flow [4,18,23], while the matrix in front of the cavity is often severely worn (Fig. 7e). In addition, the oxidation of the matrix in this severely worn area is more pronounced than that of the protected zone behind the WC particle (Rectangle 1 and 4 in Table 1 and Fig. 7d). Fractured or partially pulled out carbides (Fig. 7c) and cracked oxide patches (Fig. 8a) may also be observed [23,24]. As shown in Fig. 7b, oxide patches exhibit different contrast depending on the element present in the oxide mixture, when observed under BSE detector. In the cyclical regime, cracked oxide patches exhibit a bright contrast as they are enriched in heavy metals (Rectangle 8 in Table 1 and Fig. 8b). Interestingly, the matrix in the vicinity of cracked patches is free of oxidation (Rectangle 9 in Table 1 and Fig. 8b).

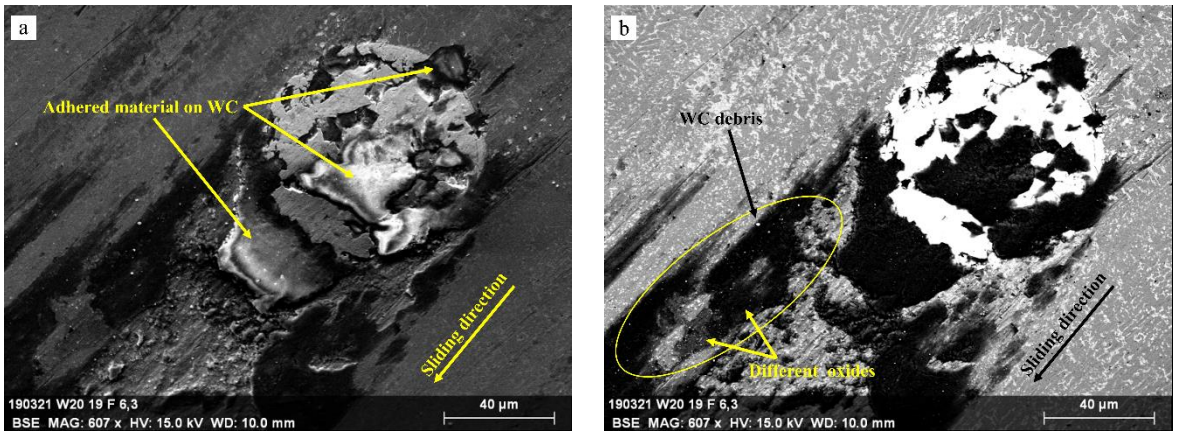

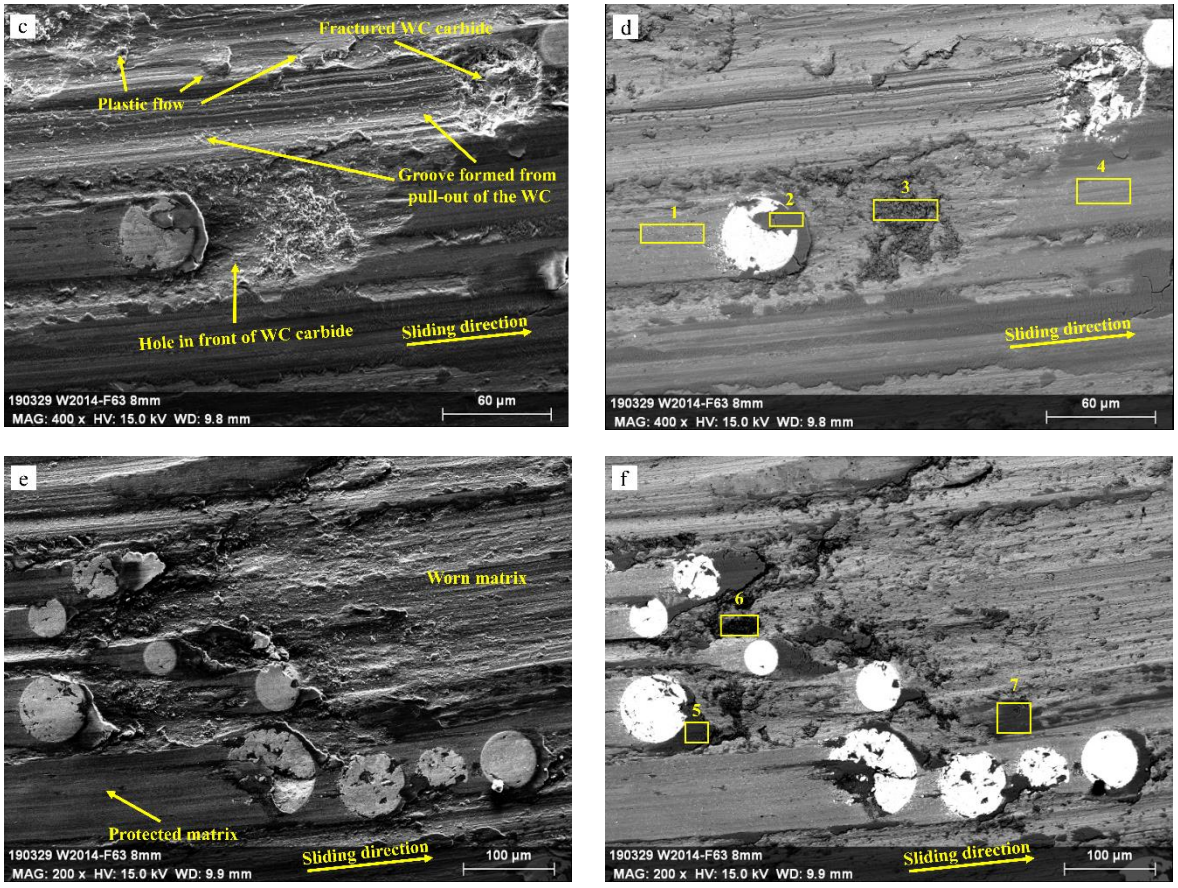

Fig. 7: SE and BSE micrographs of the typical worn surface for the first segment of the cyclical regime in the vicinities of the WC carbides, exhibiting (a and b) adhered material and different oxides, (c and d) holes, grooves and plastic flow and (e and f) the protection given by the WC carbides to the matrix.

% At.	C	O	Cr	Fe	Al	W	Ni	Mo
Point	Features in the vicinity of WC							
1	5.7	21.6	12.9	46.6	1.2	2.6	8.2	0.9
2	7.2	65.5	2.8	9.4	4.4	8.9	1.7	0.1
3	7.1	46.1	8.2	28.0	3.4	1.7	4.7	0.5
4	6.9	31.8	10.3	38.9	1.5	2.6	7.1	0.6
5	6.3	68.1	3.6	13.2	3.1	3.1	2.4	0.2
6	8.0	60.3	3.6	13.9	9.6	2.1	2.3	0.2
7	6.3	53.3	6.5	23.8	2.9	2.6	4.3	0.4
	Features of the matrix							
8	2.2	27.0	8.6	31.8	3.4	16.8	5.4	0.9
9	1.8	2.5	14.3	54.8	0.3	7.5	10.2	2.0

Table 1: Chemical composition as measured by EDS for the rectangles in Fig. 7d and f, and Fig. 8b, after pin-on-disc tests.

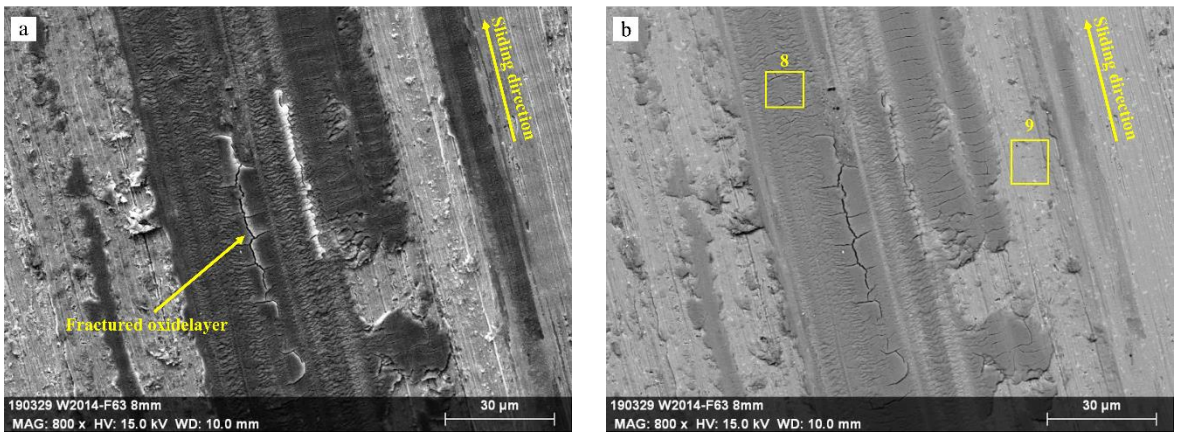

Fig. 8 : (a) SE and (b) BSE micrographs of fractured oxide patch observed after the 9300 laps test.

3.3.2.4. Cyclical regime: second segment

After test3 (Fig. 3d), the surface of the wear track (Fig. 5c) appears either smooth or with very narrow grooves that are observed far away from the WC carbides. In addition, triangular-like dark patches (Fig. 5c) are observed in front of the WC carbides, which correspond to compacted alumina debris (Fig. 9b and c). Moreover, as shown in Fig. 9a, a large quantity of small debris is well distributed on the surface. Nevertheless, the matrix is less oxidized (Fig. 9c) compared to other tests (Fig. 6e and Table 1).

Finally, the first test carried out up to 22000 cycles exhibits a worn track similar to test4 (Fig. 5d). The second test up to 22000 cycles exhibits slight differences, i.e. the worn surface is smooth with traces of dark oxides and with adhered material on the WC carbides (Fig. 5e). This difference will be discussed in section 4.2.3.

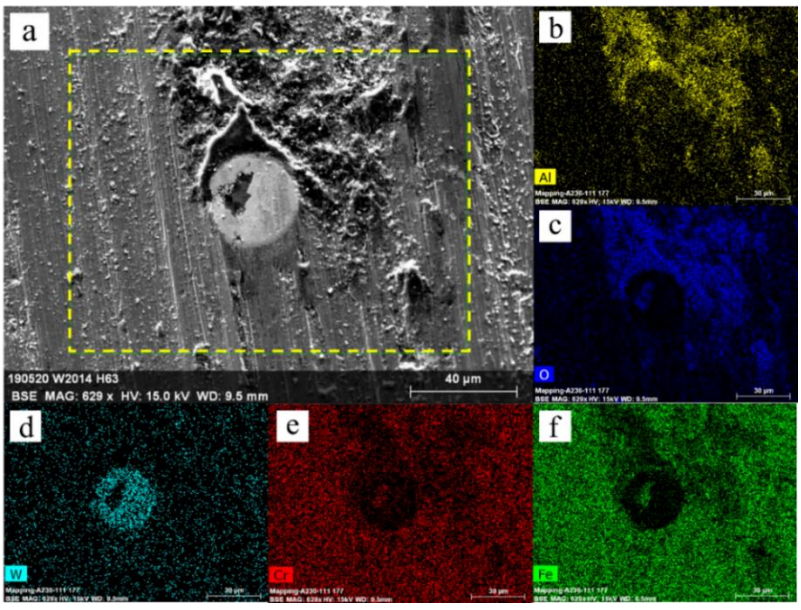

Fig. 9 : (a) SE micrograph of triangular dark patches on the wear track in front of the WC carbides, with the corresponding EDS analysis (b to f) after test4 at 11700 laps. Preferential distribution of both Al (b) and O (c) ahead of the WC reinforcement (d) due to the wear phenomenon by WC occurring within the counterbody, while both Cr (e) and Fe (f) show a more homogeneous distribution around the WC reinforcement that corresponds to the composite matrix.

3.3.3.Analysis of the cross-sections and debris within the worn samples

A 5-10 µm thick deformed layer is observed on the surface, with plastically deformed grains oriented following the sliding direction [1,5,6,26] (Fig. 10a). Meanwhile, the microstructure beneath the wear track is not perturbed [18]. The first 5 µm of this deformed layer corresponds to a crack-free mechanical mixed layer (MML) [14], where the matrix is mixed with both bright debris belonging to cracked WC carbides and fragments of solidification carbides (Fig. 2b and Fig. 10b). In the remaining 5 µm of the layer (i.e. in the subsurface) [14], solidification carbides are fragmented into small pieces due to the deformation of the matrix.

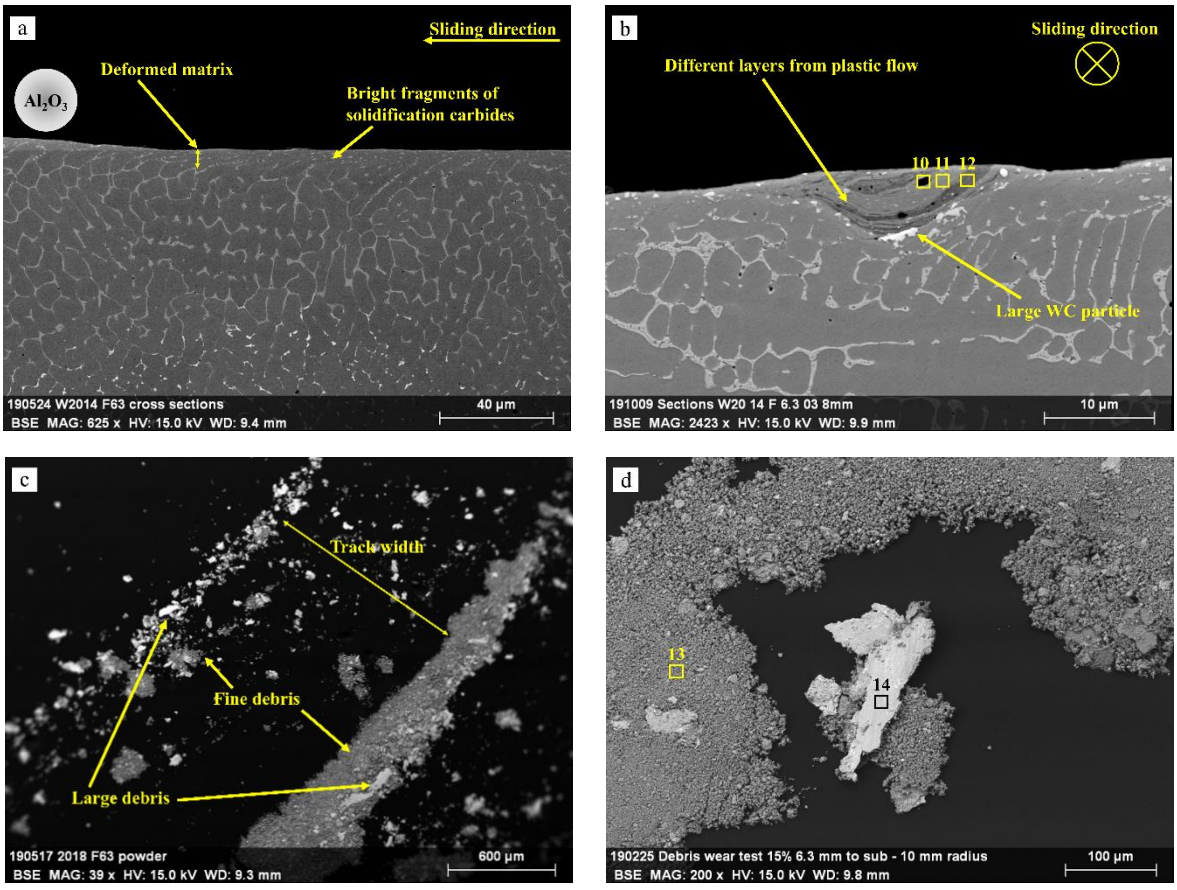

Fig. 10: Typical features of the cross-sections (a and b) and of the debris collected after the 22000 laps tests (c and d).

Furthermore, several cavities formed during the tests by pulled-out WC carbide (Fig. 7c) or delamination (Fig. 5b and c) are observed perpendicular to the sliding direction. These cavities are often filled with oxides through plastic flow (Fig. 10b) [34,48]. Three distinct oxide mixtures can be

distinguished from the BSE contrast and from the compositions listed in Table 2. Indeed, based on the works by Garza-Montes-de-Oca et al. [35] and Varga et al. [48], the MML is made of about six layers of oxides that locally form a stratified structure. Such a layered structure might be composed of alumina (Rectangle 10), a slightly oxidized matrix (Rectangle 11), and oxidized matrix + alumina (Rectangle 12).

% At.	C	O	Cr	Fe	Al	W	Ni	Mo
Point	Perpendicular cross-section							
10	5.9	49.4	3.1	9.5	29.9	0.5	1.2	0.3
11	12.2	7.0	13.4	52.7	0.1	2.4	9.3	0.9
12	9.4	40.3	8.0	31.1	1.9	2.0	5.5	0.6
	Debris							
13	6.2	14.2	11.3	45.2	4.6	11.1	7.5	/
14	25.0	8.5	10.5	44.6	0.4	1.4	9.4	0.9

Table 2: Chemical composition as measured by EDS for the rectangles in Fig. 10b and d.

The debris collected at the end of every test (Fig. 10c) are made of a mixture of fine and large fragments [21,33]. Large flake-like debris that range from 100 to 200 µm (Fig. 10d) correspond to the matrix that has been slightly oxidized (Table 1) [33]. On the other hand, much finer debris (Fig. 10d) that are mostly distributed over the external edge of the wear track are made of a mixture of oxides (Rectangle 13 in Table 2), including alumina.

4. Discussion

4.1. Influence of the original reinforcements and of the solidification carbides on the wear behaviour

The 316L+20%WC composite exhibits improved wear properties than the reference 316L. This is due to the combined effect of original WC reinforcements and of the new solidification carbides present within the austenitic matrix (Fig. 2b). As shown by works from both Lu et al. [18] and Weng et al. [22], WC carbides protect the softer metal matrix (Fig. 7c and e) from being cut by the counterbody, which impedes the abrasive wear. This protective mechanism will be further discussed in section 4.2.1. In addition, wear damages typically observed on the 316L matrix [1,3,5,6,14], such as delamination, pit, groove and material removal are also present within the composite matrix (Fig. 6a and Fig. 7c). Adhesive wear also occurs with 316L+20%WC composite leading to plastic flow within the matrix (Fig. 7c and Fig. 10b). However, the presence of the solidification carbides in the matrix of the

composite may promote abrasive wear at the expense of an adhesive wear, when compared to the reference 316L [5,22,23]. Indeed, both supersaturated solid solution and of solidification carbides increase the matrix toughness, thus leading to the formation of a thin deformed layer that follows the sliding direction (Fig. 10a) [5,47]. Fragments of solidification carbides that crack under such a severe plastic deformation enrich the MML. As demonstrated by both the works of Lanzutti et al. [6] and Li et al. [14], the presence of these particles (Fig. 10b) significantly improves the work hardening ability of the matrix since they form an efficient barrier for dislocation glide. Dislocations pile-up due to plastic deformation may eventually lead to the development of a strain gradient, and consequently to micro-cracks and delamination [14,21]. Indeed, few large flake-like debris are present after every test (Fig. 10d). The high amount of fine debris observed on the worn surfaces (Fig. 5), together with the large flakes (Fig. 10c), indicates a complex wear scenario with abrasive wear and oxidative wear as dominant wear mechanisms [14,21,33].

4.2. Elucidation of the wear sequence

The wear behaviour of complex alloys or composites often corresponds to a combination of different wear mechanisms [31–35]. This is also the case in the present study for which a complex wear behaviour of the 316L+20%WC composite has been highlighted, based on tests conducted with good repeatability. In what follows, wear mechanisms occurring within main stages of the wear sequence will be elucidated, based on the wear behaviour reported for the 316L without reinforcement [1,2,4–6,14] and on other studies of complex composite materials [17,22,27,31,32].

4.2.1. Run-in period

At the beginning of the run-in period (stage1), the surface of the specimen is still relatively rough. As a result, the actual contact area with the alumina ball – that is still unworn at this stage – is at its smallest [32], thus leading to the highest contact stresses. Plastic deformation (Fig. 5a and Fig. 10a) and adhesive wear take place for both the matrix (Fig. 6a) and the WC (Fig. 6c) due to bonding between the alumina ball and roughness within the composite surface. The formation of the MML begins at this stage (Fig. 10a). Meanwhile, the alumina ball is slightly worn either by adhesive wear [14] or by mechanical locking on the WC carbides of the composite surface (Fig. 4c and Fig. 7a), leading to a progressive

increase of the contact area together with a decrease of contact stresses. This first stage, corresponding to mild wear, is short in time. The related PDe remains almost stable during this time (Fig. 3a).

Stage2 begins when the PDe starts rising (Fig. 3c) due to an increase of the delamination (Fig. 5a and Fig. 6a) and to the damages caused on both the composite matrix and the alumina ball by 2-body abrasive wear. Indeed, the strong plastic flow and deformation of stage1 have led to the development of a strain gradient. As already shown in previous works [4,14] and explained in section 4.1, the strain gradient then causes micro-cracks and delamination of the MML in stage2, in good agreement with the presence of large debris after each test (Fig. 10c). Nevertheless, the MML is restored after delamination by continued contact with the alumina ball. The delaminated debris can oxidise and wear the softer matrix underneath, leaving grooves [5,27,37]. The combination of these different wear mechanisms leads to a high wear rate (Fig. 4b). In addition, the increase of the delamination may expose the WC carbides, thus increasing the adhesive wear of the alumina ball in contact with the hard reinforcements (Fig. 7c). On the other hand, some WC fragments (Fig. 7b) or even entire WC carbides can be pulled out (Fig. 7c) due to their enhanced exposure to the ball. The resulting large quantity of coarse and hard debris, which either come from the WC carbides or the matrix, are ground and refined (Fig. 7d) during abrasive wear (Fig. 5a), forming a first tribolayer [48,49]. As shown in Fig. 6e, oxygen is found all over the surface, thus confirming the existence of such an oxidized tribolayer.

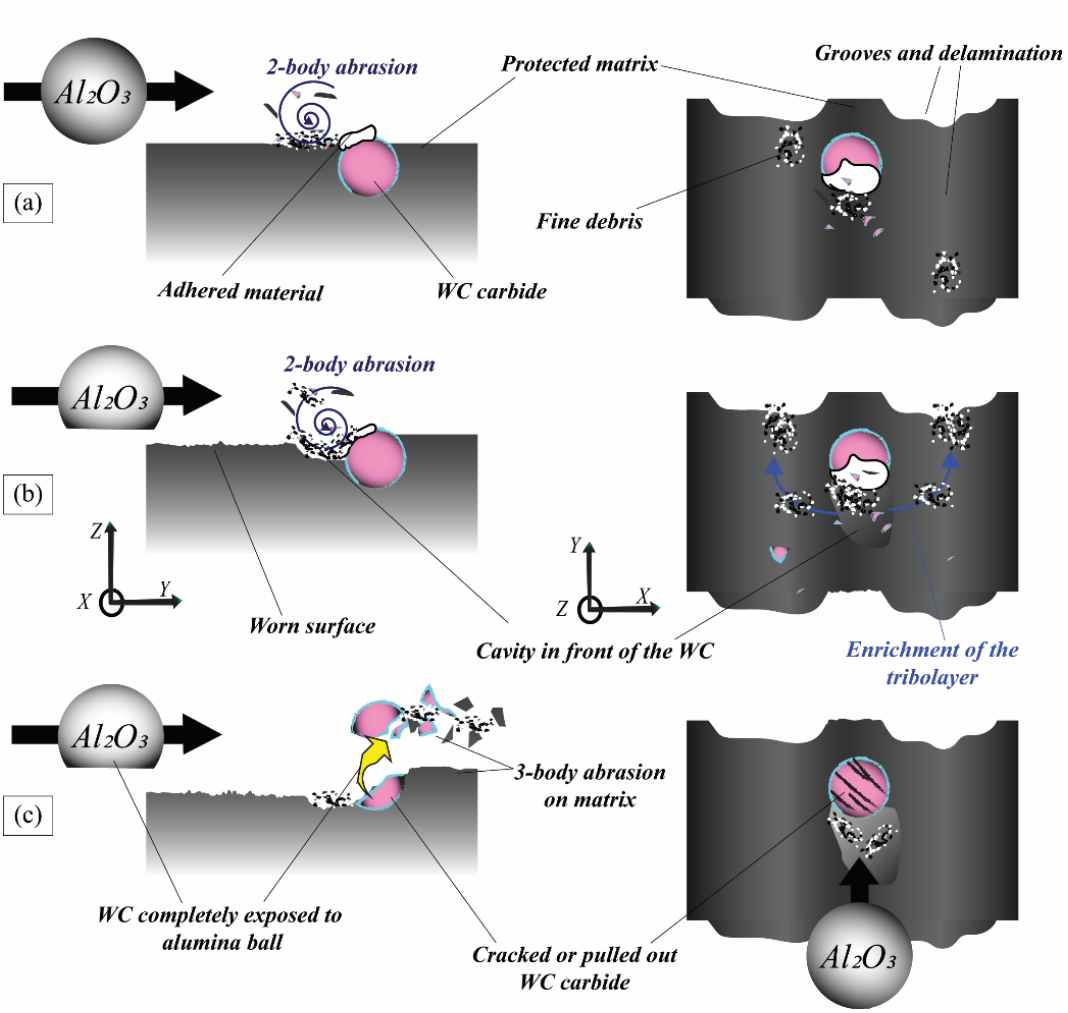

Fig. 11: Schematic of the abrasion phenomenon in front of WC carbides. (a) Beginning of the 2-body abrasion in front of the WC carbides. The ball is represented without damage (initial condition) This occurs mainly at the beginning of the test. (b) Enrichment of the tribolayer. (c) Delamination, cracking or pulling out of the WC carbides due to the high exposure to the alumina ball. In (b) and (c) the ball has been largely damaged during (a), by mechanical locking with the WC reinforcements.

In addition, WC carbides exhibit a peculiar mechanism, schematized in Fig. 11, that is in agreement with previous works [18,25]. As shown in Fig. 11a, the adhered alumina (Fig. 6c and Fig. 7b) prevents further damage to the alumina ball and acts as a barrier for debris (Fig. 7e). With the progress of the test, debris accumulates in front of the WC carbides and abrade punctually the matrix, forming a hole (Fig. 11a and Fig. 7c). This cavity increases the quantity of debris that can accumulate in this position, thus speeding up the abrasion. These debris are made of alumina with other different oxides (Fig. 7f and Table 1). Moreover, during the abrasion, some fine debris in excess can move on the WC sides (Fig. 11b, Fig. 7d and f), thickening the tribolayer [25]. It is also assumed that WC carbides can fracture more easily or get pulled out if the depth of this hole increases up to more than half of the WC diameter (Fig. 5, Fig. 7a and d), increasing the exposure to the ball load (Fig. 11c). This phenomenon can be

initiated whenever a WC particle is exposed on the surface and provided a tribolayer does not protect the track (Fig. 6c), regardless of the current wear stage.

When the tribolayer (Fig. 7d) is homogeneously distributed on the whole track (Fig. 4 and Fig. 8b), it acts as a protective layer for both the wear track and the alumina ball [1,14,48]. The peak of the CoF in stage3 should correspond to the beginning of the compaction and the stabilisation [49] of the tribolayer, which is also associated to the occurrence of a plateau for the PDe (Fig. 3e). It is worth noting that this steady-state stage does not occur when the 316L alone is tested (Appendix B, Fig. B.2). From the work by da Conceição & D'Oliveira [50], it has been found that faster oxidation kinetics contribute to form a continuous tribolayer that is more compacted and more stable than oxide clusters, and thus decrease the CoF. Therefore, it can be assumed that the peak of CoF within Stage3 represents the moment when debris on the wear track changes from uncompacted to compacted ones, which decrease the CoF. In addition to what has been previously highlighted in sub-section 3.3.2.2, it can be suggested that the CoF within the run-in period is controlled by the macroscopic grooving work of the ball against the disc. A support for that is the increase in width of the wear track during the first 750 cycles (see Fig. 5). Moreover, such an increase of the wear track width is related to an increase of the worn volume of the ball during the run-in period, and thus the contact area increases.

4.2.2. Cyclical regime

After the peak of the CoF at 2200 laps (Fig. 3a), a continuous increase of the CoF up to values that are higher than obtained within the run-in period, marks the beginning of the cyclical regime of the wear sequence. Both the monotonic increase of the CoF and the plateau of the PDe correspond to a mild oxidative wear mechanism (Fig. 12) and more specifically, to the continued compaction of the tribolayer with the progress of the test [51,52]. As shown in Fig. 4b, during the continuous increase of CoF (Fig. 3a), limited damages occur between test3 (Fig. 3d) and test4 (Fig. 3e). Indeed, within stage4, the tribolayer increases its thickness with material removed from the track, and the debris formed in the precedent stages are refined and oxidized [51,52]. The continuous increase of the CoF corresponds to the increase in the strain of the tribolayer. When the strain is too high to behold and the thickness of the tribolayer reaches the critical limit, compacted oxide patches crack (Fig. 8a) and the tribolayer breaks

[36,51,52]. The length of this period depends on the mix of oxides that form the tribolayer, and especially on their hardness and tendency to compact [4,6,48,49]. Indeed, the mix of oxides formed during pin-on-disc tests on the reference 316L does not form a protective layer due to their different nature, as confirmed by the continuous increase of the PDe during sliding (Appendix B, Fig. B.2).

At the main drop of CoF (transition between stage4 and stage5 in Fig. 12), acoustic emissions stop momentarily from being produced by the friction between the ball and the specimen (Appendix B (Fig. B.3) and Appendix C (video)). This sharp drop of CoF corresponds to the maximum compaction of the tribolayer, thus decreasing the friction between ball and specimen (or tribolayer). The absence of acoustic emissions corresponds to a minimum of the dissipation of kinetic energy as friction sounds or vibrations [43–45].

With the progress of the test in stage5, the tribolayer breaks and reforms again several times, since the debris can be replaced and moved along the track. However, this tribolayer is unstable since it is formed by already compacted debris. During this process, a large number of compacted debris is evacuated out of the track by centrifugal forces. The small decrease of the PDe and the high variability of the CoF represent this phenomenon (Fig. 3d and e), where large and compacted debris is distributed heterogeneously on the track, increasing the distance between ball and surface.

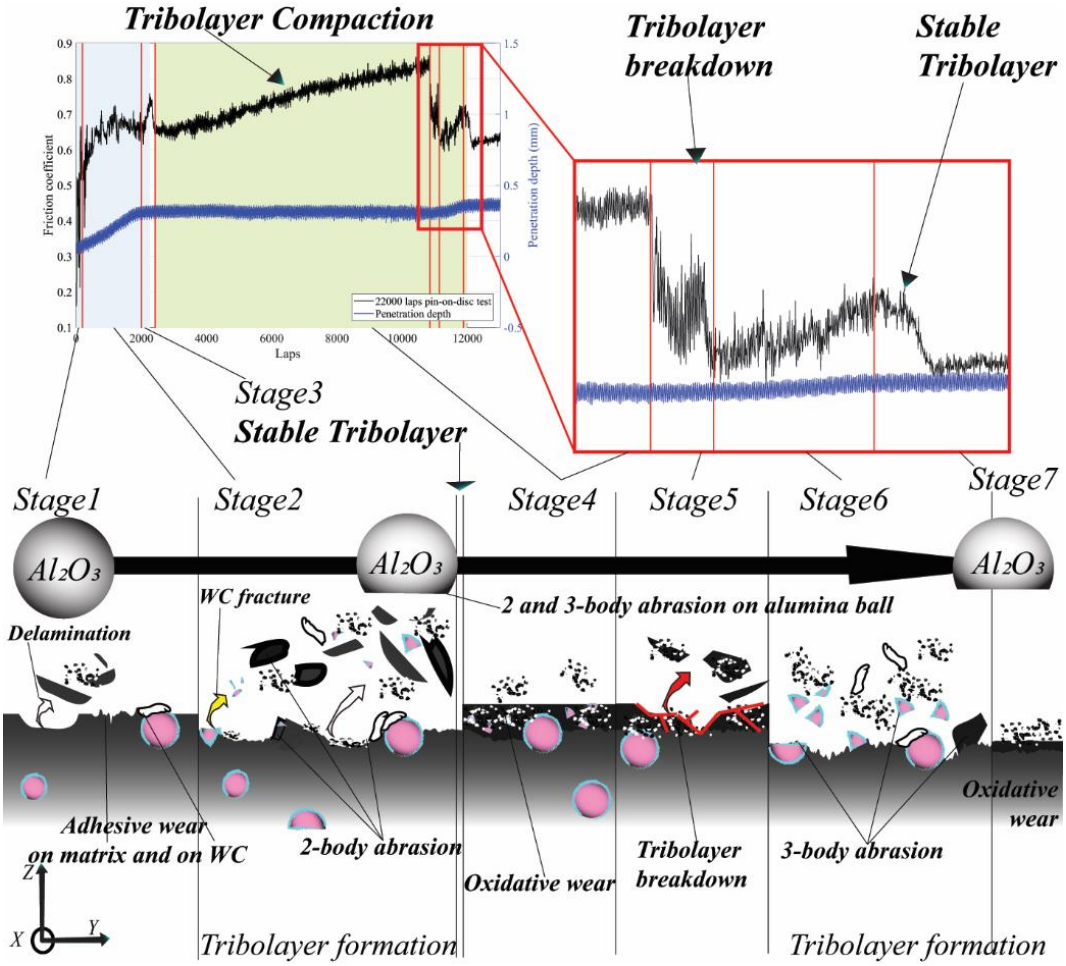

Fig. 12: Wear sequence of the 316L+20%WC composite. Each stage is associated with a part of the pin-on-disc test based on the specific variations of the CoF and the PDe. The main wear mechanisms for each stage are represented. In order to represent the wear of the track and the alumina ball, the height of the sample surface and the diameter of the ball decrease with the progress of the test.

When both CoF and PDe increase (Fig. 3d), large portion of the track surface is debris-free and the process to form a stable tribolayer restarts (Fig. 12). The main difference in comparison to the end of the run-in period (stage2) is the initial condition of the track surface. Indeed, in stage6, the contact area is increased with the progress of the test due to 2-body and 3-body abrasion [32] (Fig. 4c). As consequence, the punctual pressure of the ball is lower upon the MML that is already formed. The lower contact pressure decreases the occurrence of delamination (Fig. 10a) by limiting the development of a strain gradient. The increase of the contact area during the test depends on both the length of the oxidative stage (protecting both ball and specimen) and the amount of WC exposed on the given surface (that controls the extent of the mechanical locking). Indeed, the worn caps of the alumina balls (Fig. 4c) for the two test0 exhibit lower sizes in comparison to the worn caps for the interrupted tests. This is due to a slightly lower quantity of WC carbide in the specific 6.3 surfaces used for the test0 (see section

2.2). Furthermore, the condition of the track is also influenced by the evacuation of the tribolayer, which leaves the WC carbides more exposed to the alumina ball (Fig. 11c). Both the alumina ball and the WC carbides are worn by their contact through mechanical locking and fracture [24]. Large fragments from alumina and WC, together with some finer debris from the first tribolayer, act as third body of the 3-body abrasion, restarting the formation of a new tribolayer [49].

4.2.3. Role of the tribolayer

In Fig. 12, the stabilisation of the first tribolayer (stage3) corresponds to a complete peak in the CoF since the PDe is stable on both sides of this peak (Fig. 3a). On the other hand, as discussed in section 4.2.2, during the shorter formation (Fig. 3d) of the second tribolayer (stage6) the PDe exhibits an increase corresponding to the left part of the peak of the CoF. This variation is probably due to the different combinations of wear mechanisms that lead to the formation of debris and thus of the tribolayer. Therefore, the stabilisation of the second tribolayer is considered as part of a stage7, corresponding to a steady PDe. Indeed, the formation of the second tribolayer (stage6) is faster (Fig. 3a) than for the first tribolayer (stage2). This is due to the presence of debris on the track coming from the previous stages, and to a more regular surface (Fig. 5c) [48,49]. Test3 was stopped just after the complete stabilisation of the second tribolayer, its worn track exhibiting a smooth surface (Fig. 5c). Indeed, during stage6, the worn surface was levelled both by the contact with the alumina ball and by the abrasion due to finer debris (Fig. 10d). Furthermore, as shown in Fig. 9, debris of different nature (Table 2) can fill in the gaps left by pulled out WC carbides (Fig. 10b) or the grooves in the matrix (Fig. 5b and Fig. 7c). In particular, the triangular dark shapes observed in Fig. 5c and Fig. 9 are compacted oxides spread onto the surface (Fig. 9), filling the grooves or gaps left by previous wear stages (Fig. 11c). However, as shown by the comparison of the different surface conditions for test4 and test0 (that correspond both to stage7), the surface roughness depends on the nature of the debris formed during stage6 [37,49]. Large quantity of hard debris (from WC carbides and alumina) can increase 3-body abrasion, thus leading to a more irregular track with dark patches (Fig. 5d) [49], while intensifying the formation of the tribolayer [48,49]. In contrast, finer debris leads to an enhanced smoothening of the track (Fig. 5c and e) and to a more homogeneous and well-spread tribolayer [48].

Stage6 and the first segment of the cyclical regime finish when the second tribolayer homogenise on the track. Then, a new segment of the cyclical regime begins (Fig. 3a). Stage7 corresponds to the compaction and stabilisation of the new tribolayer (Fig. 12). This proposed wear sequence of the MMC is schematized in Fig. 12. In order to represent the wear of both the track and of the alumina ball (Fig. 4b and c), the height of the sample surface and the diameter of the ball are shown to decrease with the progress of the test. Furthermore, the main wear mechanisms for each stage are represented.

5. Conclusions

A complex hierarchical microstructure is achieved when adding 20 vol.% of WC particles within SS316L processed by DED. Under dry sliding conditions, the wear resistance of such a composite is significantly improved compared to that of SS316L, due to (partially dissolved) WC carbides and to the formation of a reinforced matrix. In particular, WC carbides protect the matrix from direct contact with the ball on the one hand, and they enrich the tribolayer during wear test on the second hand. Furthermore, as also observed in the SS316L, after an initial plastic flow of the matrix, fragments of the new solidification carbides also enrich the MML while increasing its strength, thus helping to improve the wear resistance.

The wear rate of the specimen decreases firstly and then presents no visible difference with increasing sliding time, due to the formation of a protective tribolayer. The wear rate of the counterbody also decreases with the progress of the test. The wear of the counterbody depends on the length of the oxidative stage, which protects both ball and specimen. The wear of the counterbody also depends on the amount of WC exposed on the given surface, which controls the extent of the mechanical locking of the ball. Moreover, results highlight that the nature of the counterbody, especially the nature of the debris (oxides mix), determines the tendency to form a stable tribolayer.

The interrupted tests approach has revealed important insights into the complex wear sequence of the 316L+20%WC composite, while dividing the global wear phenomena into fundamental steps. Indeed, SEM observations have shown different situations of the wear track depending on the sliding distance, which correspond to an evolution of the wear mechanisms. The wear behaviour of the 316L+20%WC composite was elucidated while considering the variations of both the CoF and the PDe, and by taking

into account the wear rate evolution and the post-mortem observations of the wear tracks. Seven different stages were distinguished regarding the wear sequence of the MMC, which are as follows:

- Two initial stages compose the initial run-in period. This period is characterized by relatively severe wear of both specimen and counterbody, which are due to delamination, adhesive wear and abrasive wear.
- Wear mechanisms of the run-in period lead to the formation of a large quantity of debris and to the formation of the first tribolayer. A cyclical regime follows, characterized by mild wear involving the repeated compaction, breakdown and reformation of the protective tribolayer.
- Both the reinforced matrix and the undissolved WC that made the complex hierarchical microstructure of the 316L+20%WC composite influence the formation of tribolayer. Such a hierarchical microstructure also influences the subsequent complex wear mechanisms that occurred under dry sliding conditions.

Appendix A: Raw material (powder feedstock) with spherical-like morphology, DED processing parameters, and DEDed 316L+WC composite sizes within the as-built conditions.

Appendix B: Cellular structure and related CoF and PDe evolution during full pin-on-disc test on DEDed 316L, and time of CoF collapsing within DEDed 316L+WC hierarchical composite during wear test.

Appendix C: Video recording the acoustic emission related to the transition between continuous increase and collapse of CoF on DEDed 316L+WC hierarchical composite under dry sliding.

6. Acknowledgements

This work has been supported by a subvention “Crédit classique” of the University of Liège, and by the European Fund for Regional Development and the Walloon Region under convention FEDER “Iawatha”. The authors acknowledge the CAREM of the ULiège for providing SEM/EDS/EBSD facilities. They also thank Sylvie Salieri, Jide Han and Benjamin Peeters for the sample preparation, Laura Zorzetto and Mattia Nordera for helpful discussion, Samuel Rondia for the substrates preparation and the Sirris Research Centre for providing access to the DEDing equipment.

7. References

[1] O’Donnell LJ, Michal GM, Ernst F, Kahn H, Heuer AH. Wear maps for low temperature carburised 316L austenitic stainless steel sliding against alumina. Surface Engineering 2010;26:284–92. https://doi.org/10.1179/026708410X12550773057901.

[2] Dearnley PA, Aldrich-Smith G. Corrosion–wear mechanisms of hard coated austenitic 316L stainless steels. Wear 2004;256:491–9. https://doi.org/10.1016/S0043-1648(03)00559-3.

[3] Guan D, He X, Zhang R, Li R, Qu X. Tribological and corrosion properties of PM 316L matrix composites reinforced by in situ polymer-derived ceramics. Vacuum 2018;148:319–26. https://doi.org/10.1016/j.vacuum.2017.12.003.
[4] Li H, Ramezani M, Li M, Ma C, Wang J. Tribological performance of selective laser melted 316L stainless steel. Tribology International 2018;128:121–9. https://doi.org/10.1016/j.triboint.2018.07.021.
[5] Song L, Zeng G, Xiao H, Xiao X, Li S. Repair of 304 stainless steel by laser cladding with 316L stainless steel powders followed by laser surface alloying with WC powders. Journal of Manufacturing Processes 2016;24:116–24. https://doi.org/10.1016/j.jmapro.2016.08.004.
[6] Lanzutti A, Marin E, Tamura K, Morita T, Magnan M, Vaglio E, et al. High temperature study of the evolution of the tribolayer in additively manufactured AISI 316L steel. Additive Manufacturing 2020;34:101258. https://doi.org/10.1016/j.addma.2020.101258.
[7] Thompson SM, Bian L, Shamsaei N, Yadollahi A. An overview of Direct Laser Deposition for additive manufacturing; Part I: Transport phenomena, modeling and diagnostics. Additive Manufacturing 2015;8:36–62. https://doi.org/10.1016/j.addma.2015.07.001.
[8] Paydas H, Mertens A, Carrus R, Lecomte-Beckers J, Tchoufang Tchuindjang J. Laser cladding as repair technology for Ti–6Al–4V alloy: Influence of building strategy on microstructure and hardness. Materials & Design 2015;85:497–510. https://doi.org/10.1016/j.matdes.2015.07.035.
[9] Köhnen P, Létang M, Voshage M, Schleifenbaum JH, Haase C. Understanding the process-microstructure correlations for tailoring the mechanical properties of L-PBF produced austenitic advanced high strength steel. Additive Manufacturing 2019;30:100914. https://doi.org/10.1016/j.addma.2019.100914.
[10] Chen H, Gu D, Kosiba K, Lu T, Deng L, Xi L, et al. Achieving high strength and high ductility in WC-reinforced iron-based composites by laser additive manufacturing. Additive Manufacturing 2020;35:101195. https://doi.org/10.1016/j.addma.2020.101195.
[11] Ho I-T, Chen Y-T, Yeh A-C, Chen C-P, Jen K-K. Microstructure evolution induced by inoculants during the selective laser melting of IN718. Additive Manufacturing 2018;21:465–71. https://doi.org/10.1016/j.addma.2018.02.018.
[12] Mertens AI. Chapter 13 - Metal matrix composites processed by laser additive manufacturing: microstructure and properties. In: Pou J, Riveiro A, Davim JP, editors. Additive Manufacturing, Elsevier; 2021, p. 409–25. https://doi.org/10.1016/B978-0-12-818411-0.00005-7.
[13] Ertugrul O, Maurizi Enrici T, Paydas H, Saggionetto E, Boschini F, Mertens A. Laser cladding of TiC reinforced 316L stainless steel composites: Feedstock powder preparation and microstructural evaluation. Powder Technology 2020;375:384–96. https://doi.org/10.1016/j.powtec.2020.07.100.
[14] Li J, Zhao Z, Bai P, Qu H, Liang M, Liao H, et al. Tribological Behavior of TiC Particles Reinforced 316Lss Composite Fabricated Using Selective Laser Melting. Materials 2019;12:950. https://doi.org/10.3390/ma12060950.
[15] Deschuyteneer D, Petit F, Gonon M, Cambier F. Processing and characterization of laser clad NiCrBSi/WC composite coatings — Influence of microstructure on hardness and wear. Surface and Coatings Technology 2015;283:162–71. https://doi.org/10.1016/j.surfcoat.2015.10.055.
[16] Maurizi Enrici T, Dedry O, Boschini F, Tchuindjang JT, Mertens A. Microstructural and Thermal Characterization of 316L + WC Composite Coatings Obtained by Laser Cladding. Advanced Engineering Materials 2020;22:2000291. https://doi.org/10.1002/adem.202000291.
[17] Torres H, Vuchkov T, Rodríguez Ripoll M, Prakash B. Tribological behaviour of MoS2-based self-lubricating laser cladding for use in high temperature applications. Tribology International 2018;126:153–65. https://doi.org/10.1016/j.triboint.2018.05.015.
[18] Lu JZ, Cao J, Lu HF, Zhang LY, Luo KY. Wear properties and microstructural analyses of Fe-based coatings with various WC contents on H13 die steel by laser cladding. Surface and Coatings Technology 2019;369:228–37. https://doi.org/10.1016/j.surfcoat.2019.04.063.
[19] Xiao Q, Sun W lei, Yang K xin, Xing X feng, Chen Z hao, Zhou H nan, et al. Wear mechanisms and micro-evaluation on WC particles investigation of WC-Fe composite coatings fabricated by laser cladding. Surface and Coatings Technology 2021;420:127341. https://doi.org/10.1016/j.surfcoat.2021.127341.
[20] Sun J, Yu H, Zeng D, Shen P. Wire–powder–arc additive manufacturing: A viable strategy to fabricate carbide ceramic/aluminum alloy multi-material structures. Additive Manufacturing 2022;51:102637. https://doi.org/10.1016/j.addma.2022.102637.
[21] Zhou S, Dai X, Zheng H. Microstructure and wear resistance of Fe-based WC coating by multi-track overlapping laser induction hybrid rapid cladding. Optics & Laser Technology 2012;44:190–7. https://doi.org/10.1016/j.optlastec.2011.06.017.
[22] Weng Z, Wang A, Wu X, Wang Y, Yang Z. Wear resistance of diode laser-clad Ni/WC composite coatings at different temperatures. Surface and Coatings Technology 2016;304:283–92. https://doi.org/10.1016/j.surfcoat.2016.06.081.

[23] Fernández MR, García A, Cuetos JM, González R, Noriega A, Cadenas M. Effect of actual WC content on the reciprocating wear of a laser cladding NiCrBSi alloy reinforced with WC. Wear 2015;324–325:80–9. https://doi.org/10.1016/j.wear.2014.12.021.
[24] Domitner J, Aigner M, Stern T, Paar A, Sommitsch C, Elizondo L. Thermomechanical Wear Testing of Metal Matrix Composite Cladding for Potential Application in Hot Rolling Mills. Steel Research International 2020;91:1900478. https://doi.org/10.1002/srin.201900478.
[25] Yan X, Chen C, Zhao R, Ma W, Bolot R, Wang J, et al. Selective laser melting of WC reinforced maraging steel 300: Microstructure characterization and tribological performance. Surface and Coatings Technology 2019;371:355–65. https://doi.org/10.1016/j.surfcoat.2018.11.033.
[26] Rodrigues ACP, Yonamine T, Sinatora A, Azevedo CRF. Pin-on-disc tribotests with the addition of Cu particles as an interfacial media: Characterization of disc tribosurfaces using SEM-FIB techniques. Tribology International 2016;100:351–9. https://doi.org/10.1016/j.triboint.2016.03.034.
[27] Vergne C, Boher C, Gras R, Levaillant C. Influence of oxides on friction in hot rolling: Experimental investigations and tribological modelling. Wear 2006;260:957–75. https://doi.org/10.1016/j.wear.2005.06.005.
[28] Łępicka M, Ciszewski A, Golak K, Grądzka-Dahlke M. A Comparative Study of Friction and Wear Processes of Model Metallic Biomaterials Including Registration of Friction-Induced Temperature Response of a Tribological Pair. Materials 2019;12:4163. https://doi.org/10.3390/ma12244163.
[29] Zou Y, Tan C, Qiu Z, Ma W, Kuang M, Zeng D. Additively manufactured SiC-reinforced stainless steel with excellent strength and wear resistance. Additive Manufacturing 2021;41:101971. https://doi.org/10.1016/j.addma.2021.101971.
[30] Nartu MSKKY, Torgerson TB, Mantri SA, Banerjee R, Scharf TW. Directed energy deposition of Ni-Al-Cr-C composites: Microstructural evolution during solidification and wear. Additive Manufacturing 2021;42:102000. https://doi.org/10.1016/j.addma.2021.102000.
[31] Li CX, Xia J, Dong H. Sliding wear of TiAl intermetallics against steel and ceramics of Al2O3, Si3N4 and WC/Co. Wear 2006;261:693–701. https://doi.org/10.1016/j.wear.2006.01.044.
[32] Zhang C, Song J, Jiang L, Gao J, Liang G, Lei C, et al. Fabrication and tribological properties of WC-TiB2 composite cutting tool materials under dry sliding condition. Tribology International 2017;109:97–103. https://doi.org/10.1016/j.triboint.2016.12.029.
[33] Ayyagari A, Hasannaeimi V, Grewal HS, Arora H, Mukherjee S. Corrosion, Erosion and Wear Behavior of Complex Concentrated Alloys: A Review. Metals 2018;8:603. https://doi.org/10.3390/met8080603.
[34] Liang X, Liu Z, Wang B. Physic-chemical analysis for high-temperature tribology of WC-6Co against Ti–6Al–4V by pin-on-disc method. Tribology International 2020;146:106242. https://doi.org/10.1016/j.triboint.2020.106242.
[35] Garza-Montes-de-Oca NF, Rainforth WM. Wear mechanisms experienced by a work roll grade high speed steel under different environmental conditions. Wear 2009;267:441–8. https://doi.org/10.1016/j.wear.2009.01.048.
[36] Dai J, Zhang X, Yin Q, Ni S, Ba Z, Wang Z. Friction and wear behaviors of biodegradable Mg-6Gd-0.5Zn-0.4Zr alloy under simulated body fluid condition. Journal of Magnesium and Alloys 2017;5:448–53. https://doi.org/10.1016/j.jma.2017.11.002.
[37] Hashemi N, Mertens A, Montrieux H-M, Tchuindjang JT, Dedry O, Carrus R, et al. Oxidative wear behaviour of laser clad High Speed Steel thick deposits: Influence of sliding speed, carbide type and morphology. Surface and Coatings Technology 2017;315:519–29. https://doi.org/10.1016/j.surfcoat.2017.02.071.
[38] Zhu L, Wang S, Pan H, Yuan C, Chen X. Research on remanufacturing strategy for 45 steel gear using H13 steel powder based on laser cladding technology. Journal of Manufacturing Processes 2020;49:344–54. https://doi.org/10.1016/j.jmapro.2019.12.009.
[39] Tan C, Ma W, Deng C, Zhang D, Zhou K. Additive manufacturing SiC-reinforced maraging steel: Parameter optimisation, microstructure and properties. Advanced Powder Materials 2023;2:100076. https://doi.org/10.1016/j.apmate.2022.100076.
[40] Candel JJ, Amigó V, Ramos JA, Busquets D. Sliding wear resistance of TiCp reinforced titanium composite coating produced by laser cladding. Surface and Coatings Technology 2010;204:3161–6. https://doi.org/10.1016/j.surfcoat.2010.02.070.
[41] Kundu S, Hussain M, Kumar V, Kumar S, Das AK. Direct metal laser sintering of TiN reinforced Ti6Al4V alloy based metal matrix composite: Fabrication and characterization. Int J Adv Manuf Technol 2018;97:2635–46. https://doi.org/10.1007/s00170-018-2159-7.
[42] Feenstra DR, Cruz V, Gao X, Molotnikov A, Birbilis N. Effect of build height on the properties of large format stainless steel 316L fabricated via directed energy deposition. Additive Manufacturing 2020;34:101205. https://doi.org/10.1016/j.addma.2020.101205.

[43] Akay A. Acoustics of friction. The Journal of the Acoustical Society of America 2002;111:1525–48. https://doi.org/10.1121/1.1456514.
[44] Downey J, O'Leary P, Raghavendra R. Comparison and analysis of audible sound energy emissions during single point machining of HSTS with PVD TiCN cutter insert across full tool life. Wear 2014;313:53–62. https://doi.org/10.1016/j.wear.2014.02.004.
[45] Cai Z, Guan H, Chen Z, Qian H, Tang L, Zhou Z, et al. Impact fretting wear behavior of 304 stainless steel thin-walled tubes under low-velocity. Tribology International 2017;105:219–28. https://doi.org/10.1016/j.triboint.2016.10.002.
[46] Samuel. S C, M Arivarasu, T. RP. High temperature dry sliding wear behaviour of laser powder bed fused Inconel 718. Additive Manufacturing 2020;34:101279. https://doi.org/10.1016/j.addma.2020.101279.
[47] Kazemi M, Saghafian H. Application of response surface methodology in determining the optimal wear properties of the titanium carbide reinforced AISI H13 hot working tool steel fabricated by pulsed laser method. Surface and Coatings Technology 2020;404:126478. https://doi.org/10.1016/j.surfcoat.2020.126478.
[48] Varga M, Rojacz H, Winkelmann H, Mayer H, Badisch E. Wear reducing effects and temperature dependence of tribolayer formation in harsh environment. Tribology International 2013;65:190–9. https://doi.org/10.1016/j.triboint.2013.03.003.
[49] Costa HL, Oliveira Junior MM, de Mello JDB. Effect of debris size on the reciprocating sliding wear of aluminium. Wear 2017;376–377:1399–410. https://doi.org/10.1016/j.wear.2016.10.025.
[50] Conceição L da, D'Oliveira ASCM. The effect of oxidation on the tribolayer and sliding wear of a Co-based coating. Surface and Coatings Technology 2016;288:69–78. https://doi.org/10.1016/j.surfcoat.2016.01.013.
[51] Stachowiak GW, Batchelor AW. Engineering Tribology. Butterworth-Heinemann; 2013.
[52] Brizmer V, Matta C, Nedelcu I, Morales-Espejel GE. The Influence of Tribolayer Formation on Tribological Performance of Rolling/Sliding Contacts. Tribol Lett 2017;65:57. https://doi.org/10.1007/s11249-017-0839-3.